The Veto System Pulser and Studies of Deep Underground Muons for the CDMS-II Experiment

by

Robert H. Nelson

A dissertation submitted in partial satisfaction of the
requirements for the degree of
Bachelors of Science

in

Physics

in the

COLLEGE OF LETTERS AND SCIENCE
of the
UNIVERSITY OF CALIFORNIA, SANTA BARBARA

Advisor:
Harry N. Nelson

Spring 2003

The dissertation of Robert H. Nelson is approved:

Harry N. Nelson   6/12/03

_____
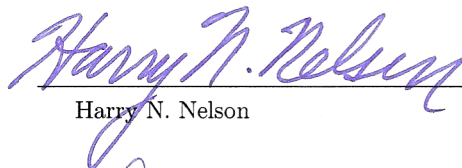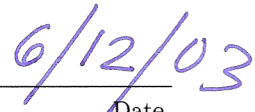
Harry N. Nelson   Date

_____

Claudio Campagnari   6/16/03
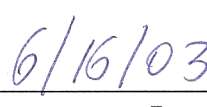
Claudio Campagnari   Date

_____

Deborah Fygenson   6/13/03

Deborah Fygenson   Date

University of California, Santa Barbara

Spring 2003

The Veto System Pulser and Studies of Deep Underground Muons for the CDMS-II Experiment

Abstract

The Veto System Pulser and Studies of Deep Underground Muons for the
CDMS-II Experiment

by

Robert H. Nelson

Bachelors of Science in Physics

University of California, Santa Barbara

Harry N. Nelson, Advisor

We describe an LED pulser constructed to calibrate the CDMS II veto shield during operation. This device pulses light into the veto shield via 40 fiber optic cables that couple to the shield through acrylic prisms. The pulser has been designed to be remote operable, and is stable at the $\sim 3\%$ level.

We have employed part of the CDMS II veto shield to measure the depth and muon flux at the Soudan mine. The depth was measured by analyzing the shape of the energy deposition spectrum in a piece of scintillator. The depth the of site is 2191 ± 162 m.w.e. The flux was measured by counting the rate through the scintillator. The flux is

$$\Phi_\mu = 2.21 \pm 0.03^{+0.00}_{-0.10} \times 10^{-3} \ \mathrm{m}^{-2} \ \mathrm{s}^{-1}$$

with vertical flux intensity

$$I_v = 1.86 \pm 0.05^{+0.00}_{-0.08} \times 10^{-3} \ \mathrm{m}^{-2} \ \mathrm{s}^{-1} \ \mathrm{sr}^{-1}$$

Acknowledgments

I would like to first thank the entire CDMS collaboration for providing me with an opportunity that I don't believe I could have found anywhere else. There are a lot of individuals that I would like to thank and I am sorry if I forget anyone. I would like to first thank 'Cosmic' Ray Bunker for putting up with me for so long, and for treating me as an equal during this project. Also for the countless times we drank beer and scotch together in order to make the pain of being in northern Minnesota a little easier. To Dan Bauer, our fearless project manager, for being the first person to decide that I should go to Minnesota where I would need the scotch. To Steve Yellin for all the time he spent helping me understand the concept of flux, and for ideas on how to do the MC. To the UCSB graduate students Joel Sander, Chris Savage, and Ron Ferril, for answering the 1000 and a half stupid questions I've asked. To Rupak Mahapatra for introducing me to some decent Indian food. To Clarence Chang and Walter Ogburn for always busting my balls for being an undergrad. To Paul Brink for making me realize that I never ever want to have anything to do with a dilution refrigerator. I would also like to thank Dave Hale and Dan Callahan who I know wouldn't trust most graduate students with a hammer, but trusted me to use just about whatever I needed. To Sam Burke for helping me design the circuit for the pulser. To Claudio Campagnari for encouraging me to write a thesis, and then asking a lot of questions during my defense, I really learned a lot. To Deborah Fygenson for being my undergraduate advisor. To Lars Bildsten for teaching my favorite class and then writing one of my grad school letters. To the existence of dark matter, otherwise this project would not have existed.

Most of all I would like to thank Harry N. Nelson (no relation) for being my advisor. I don't think that I could have had a better advisor, and I don't think the novelty both of us having brothers of each others name ever wore off.

To my parents for never forcing me to do anything in my life, but always supporting the choices I have made.

Forward

Part I of this work describes at length what has been done to create a remotely operable calibration system for the CDMS II veto shield, with a very brief overview of dark matter and the CDMS II experiment. The veto pulser is described in Chapter 4.

Part II describes depth and muon flux measurements that were made using part of the CDMS II veto shield as a muon telescope. The depth was measured using a new method fully described in Chapter 7 with the results summarized on Table 8.1. Measuring the muon flux was done in a straight forward manner and is thoroughly described in Chapter 9, with the results summarized in Table 9.3.

iv

Contents

List of Figures

viii

List of Tables

Part I

Dark Matter and CDMS II

Chapter 1

Introduction

An interesting yet unsolved problem in astro-particle physics is the nature of dark matter, an unknown type of particle that appears to make up most of the matter in the Universe. Recent results from the WMAP collaboration yield the baryon mass density of the Universe, relative to density needed to close the Universe, of $\Omega_b = 0.047 \pm 0.006$, and for dark matter mass density, $\Omega_m = 0.29 \pm 0.07$ [1]. Consequently, the fraction of matter in the Universe from baryons, R, is

$$R = \frac{\Omega_b}{\Omega_m} = 0.16 \pm 0.04. \tag{1.1}$$

Only 16% of the matter of the Universe is in the form of normal baryonic matter. The rest exists in an unknown *non*-baryonic form.

The current favored candidate for dark matter is a *Weakly-Interacting-Massive-Particle* (WIMP). WIMPs never interact via electromagnetic or strong nuclear forces, they only interact gravitationally and weakly. Astrophysically the dominant consequences arise from the gravitational interaction between dark matter and normal matter. Locally the only consequence of dark matter comes from the weak interaction, causing the rare recoil of a nucleus from an impinging WIMP.

There has yet to be a laboratory conformation of this elusive dark matter. Currently there are a number of experiments trying to directly detect dark matter

through the detection of nuclear recoils. The Cryogenic Dark Matter Search (CDMS), now in its second incarnation, known as CDMS II, is just one of the many groups looking for dark matter. The CDMS II experiment will be more thoroughly described in Chapter 2.

This work does not intend to argue for the existence of Dark Matter. We will describe the CDMS II experiment and how we hope to see dark matter, and we will discuss an interesting element of that experiment: the blue light pulser used to calibrate the muon veto shield. In Part II we will describe the measurement of the muon flux and depth of the CDMS II site, by using a part of the muon veto shield as a muon telescope.

Chapter 2

The CDMS II Experiment

2.1   Overview

The CDMS II experiment is an attempt to directly detect candidate dark matter particles known as WIMPs. The experiment uses detectors of crystals at cryogenic temperatures in which phonons created by the recoils of nuclei pushed by WIMPs are detected. These detectors are also capable of measuring the ionization created due to these interactions. Cryogenic temperatures are needed because of the needed energy resolution of about ~keV for a kg size detector [2].

The detectors used in CDMS II to detect dark matter are known as ZIPs (for Z-Dependent Ionization and Phonon) [2]. The These detectors are fabricated either from silicon or from germanium. The detectors have phonon sensors on one side with charge collection electrodes on the other, as shown in Figure 2.1. A small bias voltage $\sim 3V$ is applied across the crystals in order to facilitate the transport of ionized electrons to the electrodes. The phonon sensor is divided up into four quadrants, which are used to determine the X-Y position. The rise time of the athermal phonon pulses determines the Z position. This allows for a fiducial volume cut to reduce the leakage of surface events, mostly electrons from beta decay, from the candidate nuclear recoil events. A great deal of effort went in to understanding

backgrounds in order to be able to distinguish WIMP signals from backgrounds on an event by event basis. The rejection efficiency of a dangerous background, that of Compton scattering in the detector by environmental γ-rays, is $> 99.98\%$ for recoil energies between 5-100 keV, and for electrons from β-decay is $> 99\%$ above 10 keV [3].

Figure 2.1: A photo of a ZIP detector. Shown is the phonon channel side. Each ZIP is 1 cm thick, and 7.62 cm in diameter.

Surrounding the cold volume of the CDMS II detectors are several layers of both active and passive shielding, going outward, see Figure 2.2. The passive shielding consists of 3" of polyethylene surrounded by 2.25" of low radioactivity ancient lead, from a French shipwreck, then surrounded by 7.125" of normal lead from the Doe Run mine. Ancient lead that has been in deep water has lost most of its natural and cosmogenic radioactivity, and the normal lead from the Doe Run mine has a relatively low amount of activity for freshly mined lead. And finally a 15.5" layer of polyethylene. The final layer of shielding is an active muon-veto scintillation shield which will be described more thoroughly in Chapter 3.
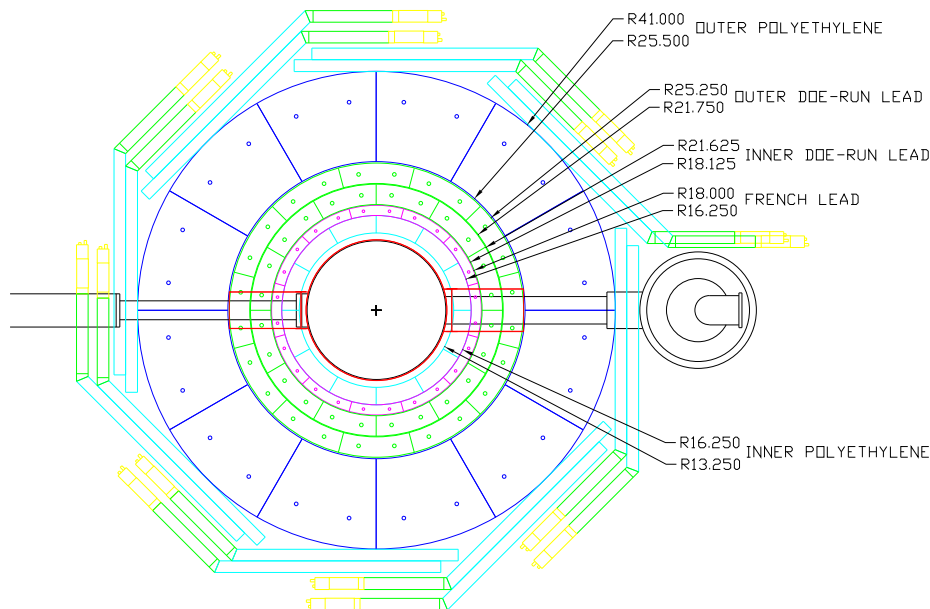
Figure 2.2: Top view of the CDMS II shield. The inner red circle is the ice box. The turquoise layer surrounding the ice box is the 3" of polyethylene. Next outward, the purple layer is the 2.25" of lead from a French shipwreck. This is surrounded by 7.125" of lead from the Doe Run mine in Missouri, the Green layer, and finally by 15.5" of polyethylene, the blue layer. The octagon shaped thing on the outside of the polyethylene shield is the active muon-veto shield. See Figure 3.1 for a more intuitive drawing.

2.2   The Soudan Mine

The CDMS II experiment is located at the bottom of the Soudan iron mine in Northern Minnesota, about half way between the towns of Virginia and Ely Minnesota. The experiment is on the 27th level (2341 ft deep) of the mine where both the Soudan II and Minos experiments are situated.

The overburden of 2341 ft of rock provides a large amount of shielding from cosmic rays, essentially reducing the atmospheric muon flux roughly by a factor of

$1.4 \cdot 10^5$. Muons induce the background that most resembles a WIMP signal. When a muon undergoes a high momentum transfer scatter off a nucleus in the matter surrounding the CDMS II experiment, often that nucleus breaks up, and liberates neutrons that penetrate into the dark matter detectors. These neutrons sometimes cause the Si or Ge nuclei in the dark matter detectors to recoil, mimicking a nuclear recoil from a WIMP interaction.

The rate of this type of background can be deduced from a good knowledge of the depth of the Soudan mine, and from a knowledge of the muon flux in the Soudan mine. Both of these quantities have been measured for this work.

2.3   Physics Goals

The CDMS II experiment is trying to narrow down the parameter space allowed for the inclusion of dark matter as a minimal extension of the Standard Model of particle physics. By measuring the energy of the elastic scatter, CDMS hopes to measure the WIMP-nucleon spin-independent cross section (σ), and the WIMPs mass (M). Typical exclusion plots for Dark Matter searches are shown as a σ vs M plot. Figure 2.3 shows the current state of the WIMP search for several different experiments [3].

The results shown for CDMS II are from a preliminary version of the experiment, which took place at Stanford in a tunnel only $30\,\text{ft}$ below the earth's surface. The sensitivity was limited by a background of neutrons, which were induced by cosmic ray muons. The increased rock overburden at the Soudan mine should suppress this background and allow sensitivity to σ about 2 orders of magnitude greater than at Stanford.
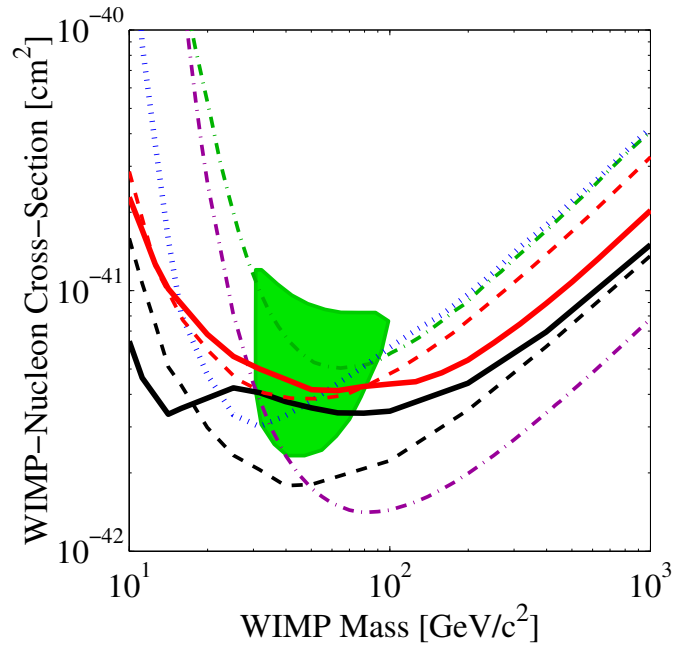
Figure 2.3: The current limits for the CDMS II experiment. The solid black line represents the current limit with neutron subtraction. The solid red line is the current limit with out neutron subtraction. The red and black dashed lines represent the expected limits. The blue dotted curve is the previous CDMS limit. The green region is the DAMA 3σ allowed region, with the green dot-dashed curve as their limit[4]. The purple dot-dashed curve is the result from the EDELWEISS experiment[5]. All are excluded at 90% CL. This is Figure 4 from [3].

Chapter 3

The Muon-Veto Shield

3.1 Design

The CDMS II muon-veto shield, shown in Figure 3.1, has been designed to provide almost complete coverage of the polyethylene shield, while being as compact as possible. This shield has been segmented into 40 separate panels, of three main geometries; the larger top panels, the bottom panels, and the angled side panels. The shield also includes small panels located at the access tubes for electronic and cryogenic services, to cover the cracks created by those holes in the shield. Finally, on the bottom there are two narrow "crack" counters that serve to cover a small gap created by the support structure. The shield has been designed so that there are no paths that pass through the dark matter detector volume without passing through at least one scintillator.

Each veto panel, as shown in Figure 3.2, is constructed out of a rectangular piece of scintillator [6] with a triangular acrylic light guide at one end. At the top of the light guide is a Hamamatsu R329-02 photo-tube [7] snugly enclosed in a cylindrical mu-metal shield. To prevent light leaks the panels are completely covered with several protective layers of material. The innermost layer is made of aluminized mylar. The next layer is made of black plastic and is covered by a layer of black

paper. Finally the panel is wrapped up in layers of black tape. To ensure that as little damage as possible happens to the veto panels during their installation, an aluminum guard has been mounted on the edges of the scintillator and around the photo-tube.
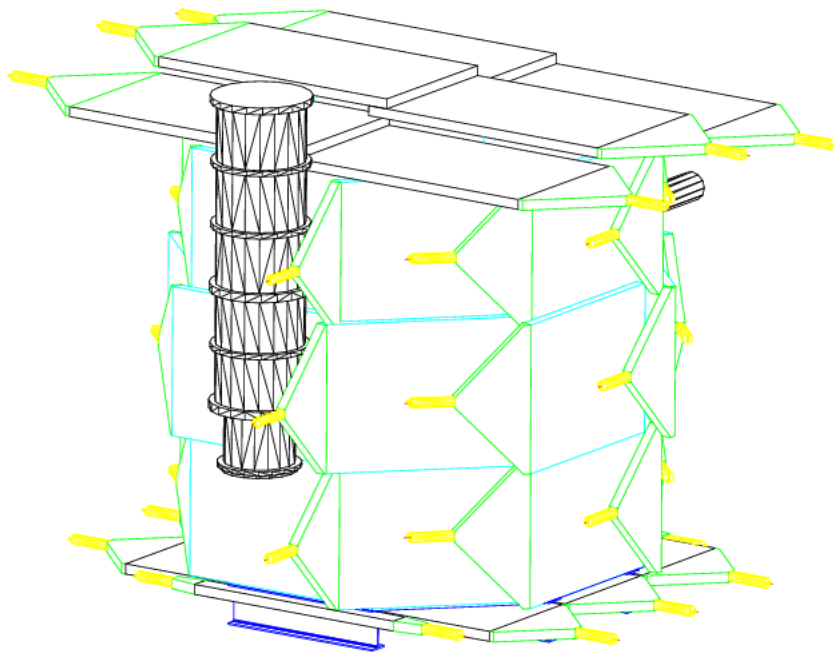
Figure 3.1: A drawing of the CDMS II veto shield. The height is a bit under three meters. The actual installation differed slightly from this drawing by having the six bottom panels facing with their photo-tubes pointing inward, so that they can not be easily damaged.

The shield is designed to be taken apart whenever access is needed into the detector volume. This involves the removal of the top panels, and the upper row of side panels. The remaining panels remain in place while access is granted.

Hopefully, this will only be necessary for the installation of new detector towers. The top portions of the polyethylene and Pb shields have been constructed to be lifted off of the shield with the help of a crane.

Figure 3.2: A drawing of a veto panel. The large rectangular portion is the scintillator. The triangular part on the right is an acrylic light guide, and the yellow cylinder is the photo-tube.

3.1.1 Implementation

The veto will be used to tag muon events coincident in time with dark matter detector (ZIP) signals. This veto will facilitate the identification of events that may be associated with an incident muon, and thus not originating from recoils due to dark matter.

The veto-panels have all been calibrated at the surface by adjusting the high voltage on the photo-tubes until the gap in signal between the γ-rays and the muons was approximately $100\,\mathrm{pC}$ of the measured charge. The panels were then checked with a $^{137}\mathrm{Cs}$ X-ray source at the centers of there geometries, and the currents were

recorded. This calibration was meant to be used so that we could check the panels after they went underground to see if anything had broken or changed.

Chapter 4

The Blue Light Pulser System

4.1   Construction and Design Goals

The blue light pulser system is a device used to keep a running calibration of the muon-veto. Unlike the ^{137}Cs source measurements, the pulser has to be able to calibrate the shield at the touch of a button. The following constraints were imposed on the design of the veto pulser:

- It must not introduce noise into the RF shielded room.

- It should be stable to the 5% level.

- It should provide uniformity between the channels.

- It should be remotely operable.

These constraints led to the design of a LED (light emitting diode) pulser that coupled to the shield through fiber optic cables.

The LEDs are from Nichia and have a peak luminosity at 470 nm [8]. Blue light is required because the Hamamatsu R329-02 photo-tubes used in the veto are sensitive to blue light alone, with a peak sensitivity at 420 nm [7]. An array of 97 LEDs are attached to the end of an acrylic cone which couples to the fiber optic

array, shown in Appendix A figures A.1 and A.2, which fans out to the 40 individual shield panels.

The driving circuit for the pulser consists of a dual one-shot that creates a square pulse train. This train gets amplified and sent to the gate of a MOS-FET (*Metal-Oxide-Semiconductor-Field-Effect-Transistor*) that delivers the 6 amps of current the LEDs need, see Figure A.4. The frequency, width, and height of the pulses can all be adjusted by trim-pots accessible through a panel on the back of the pulser box. The pulser is activated by turning on a 5 volt line that is tied to the one-shot achieving our remote operation criteria. The pulser operates at a duty cycle just below 1% duty cycle, to prevent overheating and to maximize the LED lifetime. The width of the pulses is between 50-100 ns with an amplitude of 6-8 volts. The LEDs are specified for 4 volts, however, for very short pulses must exceed this value to get sufficient light yield.
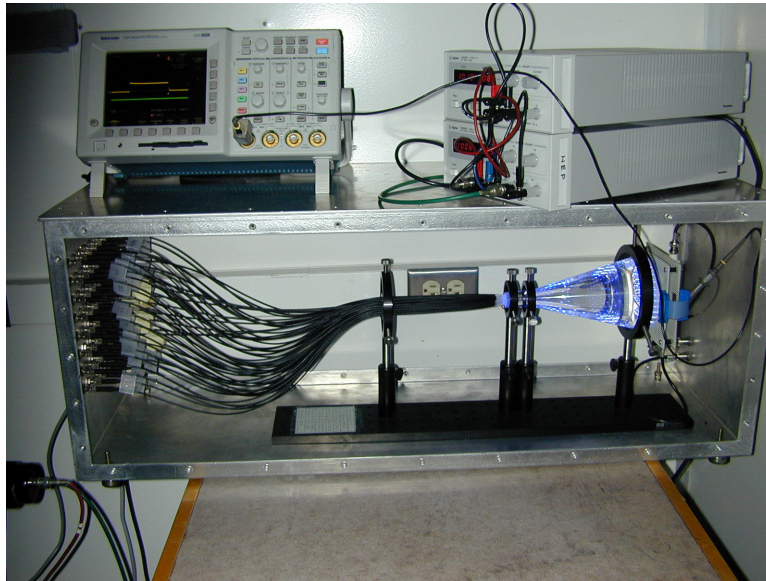
Figure 4.1: A photo of the pulser box with the side panels removed.

The pulser is located inside an RF shielded box in the electronics room of the experiment as shown in Figure 4.1. A total of 45 60' long $1000\mu m$ diameter fibers pass from the pulser through the RF shield to the muon-veto in the clean room, as shown in Figure 4.2. The fibers attach to the panels through a connector located on the side of the PMT guard, and to the pulser through a connector on the pulser box.
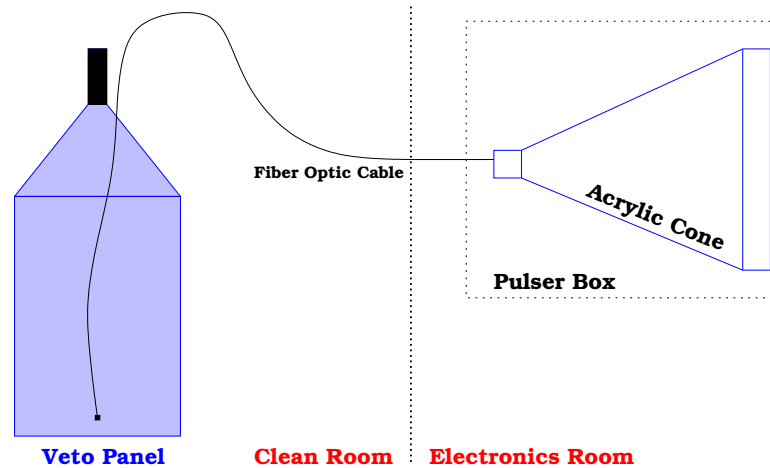
Figure 4.2: The Pulser is setup inside the electronics room of the experiment. A total of 45 fiber optic cables pass from the acrylic cone, through a pipe into the clean room, and out to a prism on each veto panel.

4.1.1   Monitoring

In order to monitor the veto pulser itself, two of the fibers have been sent to a custom photo-diode readout circuit, as shown in Figure A.5. This circuit is used to monitor the light output of the pulser as a function of time. Three fiber optic connectors have been modified to house the photo-diodes allowing the fibers to sit securely when attached to the monitoring circuit.

Three Hamamatsu photo-diodes were tested for use for the monitoring circuit. Each was placed inside a fiber connector and each viewed the same optical fiber channel from the pulser during the tests. Table 4.1 is from Hamamatsu [7],

and shows the characteristics of the three diodes. S5973-02 seems to be the best choice, however, its relatively small collection area lowered the output current which made changes in light more difficult to detect. We also placed a wavelength shifting material between the fiber from the LED and the S5972 diode, to see with if we could increase the signal. While this improved the efficiency, the light *loss* due to attenuation reduced the output signal. The model S5971 is the same as S5972 except that the S5971 has a larger collection area, and would have been the best choice. The S5971's were not available, however, so we chose the S5972's.

Table 4.1: Comparison of three Hamamatsu photo-diodes. S is the photo sensitivity in units [Area/Watt], and $QE \propto S \times$ (photon energy) is the quantum efficiency in percent. They are shown for three separate wave lengths; the wavelength of the LEDs, the wavelength of the LEDs after passing through wavelength shifter, and the wavelength for green light.

Diode	Active Area (mm^2)	S (470 nm)	QE %	S (500 nm)	QE %	S (530 nm)	QE %
S5971	1.1	0.21	55	0.24	60	0.29	68
S5972	0.5	0.21	55	0.24	60	0.29	68
S5973-02	0.12	0.35	91	0.36	89	0.37	86

4.2   Calibration and Stability Tests

4.2.1   Long Term Stability

The veto pulser was run every for ten minutes every 8 hours over a period of about 6 months. The pulser was monitored by using two of the photo-diodes, and one of the veto panels (panel #5). All outputs were monitored using the data acquisition system described in Section 6.2. The resulting charge spectra were then analyzed by finding the mean and standard deviation. The means were then plotted vs time in Figure 4.3, with their standard deviations. Except for a few unknown fluctuations, and gaps in the sequence due to down time, the run was stable at roughly the 3%

level, exceeding our design constraints.
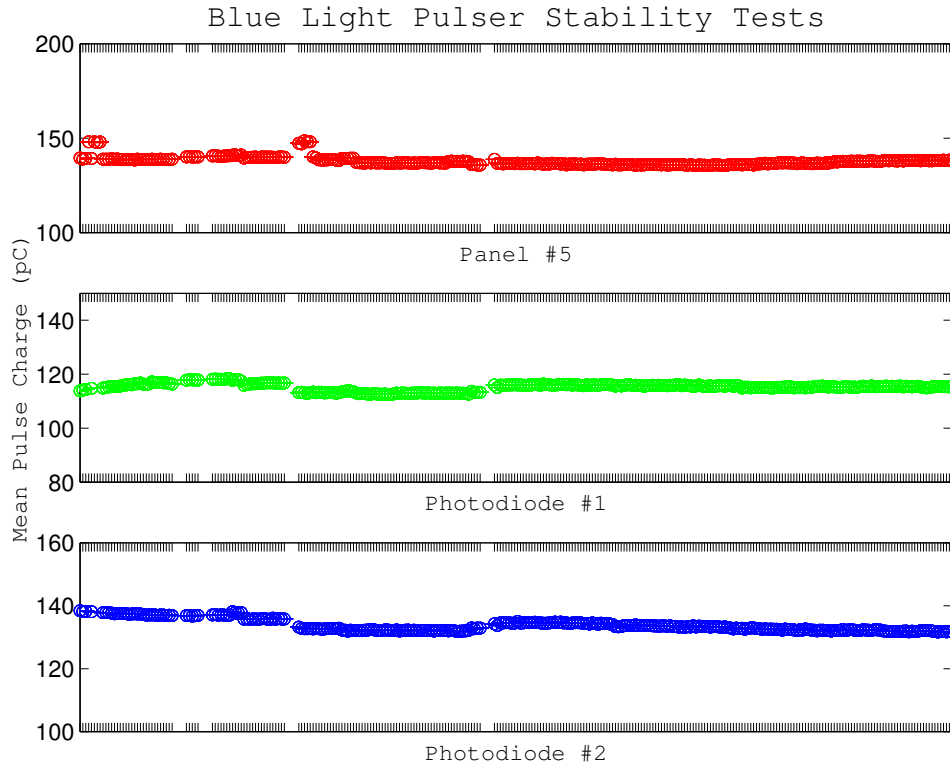
Figure 4.3: Pulser stability, from June 24th through December 2nd 2002. We ran the pulser for 16000 events at a time every 8 hours. The resulting histograms of light output were recorded, and the mean and standard deviations were measured. This plot shows the mean over this 6 month period, for veto panel #5 and two of the monitoring photo-diodes. The results show that the pulser is stable at the 3% level. Note the suppressed zero in the vertical.

4.2.2   Uniformity

The most drastic source of non-uniformity seems to be from the fiber connectors. Several types were tried, but we settled on the metallic ST style connectors from AMP (part #504021-x, where $1 \leq x \leq 4$) [9]. The non-uniformity did not change after the connectors settled, which leads us to believe that the light intensity

won't change between connections.

After the pulser's location had been finalized and all of the fibers had been attached a uniformity map was made, as shown in Figure 4.4. This figure was made by measuring the light output of each fiber off the pulser box with the same photodiode monitoring circuit. From this map, we can decide how to attach the fibers to the shield so that each panel receives a reasonable amount of light from the pulser. This will be done in a future trip to the Soudan mine.
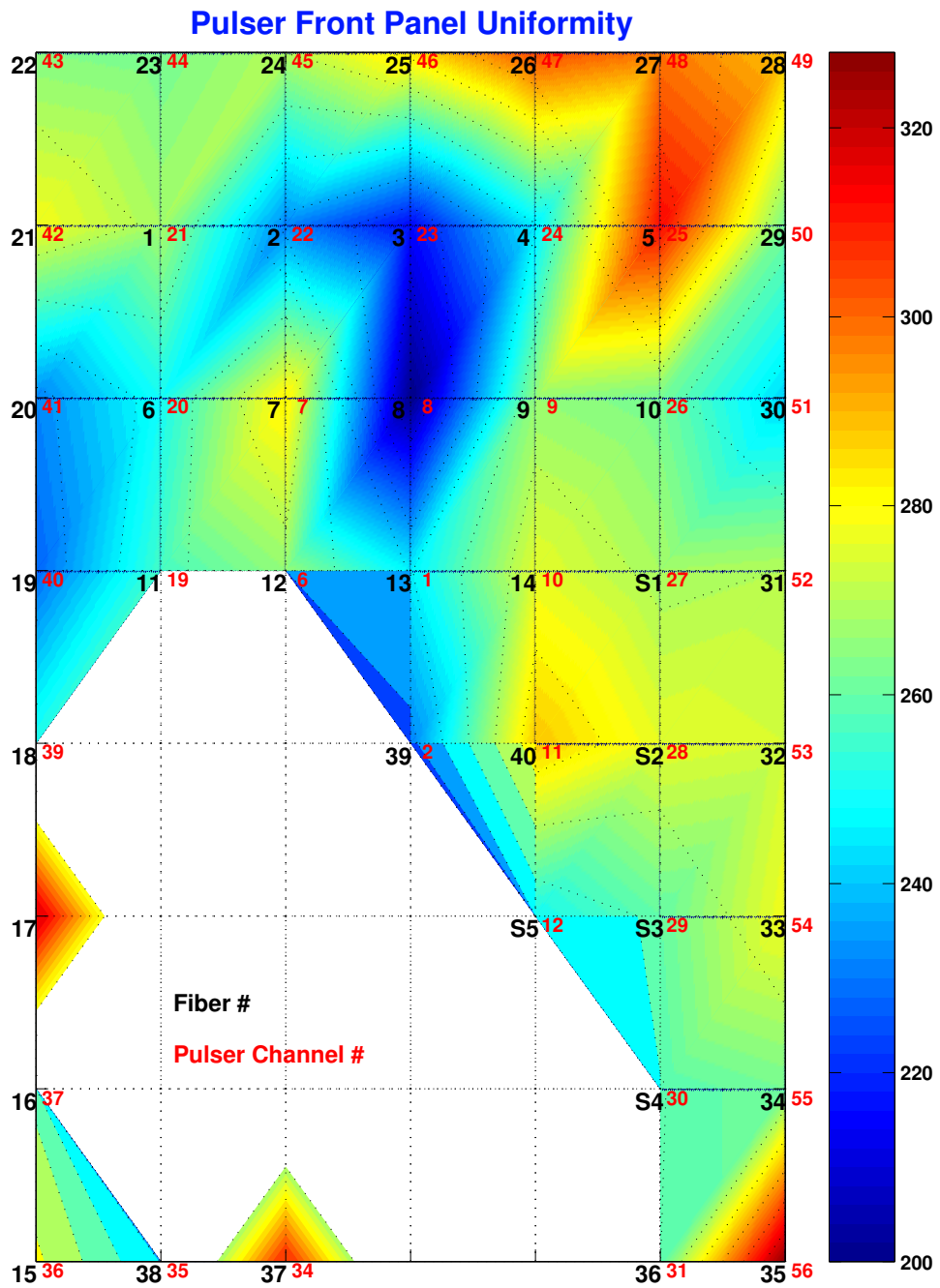
Figure 4.4: Uniformity map for the pulser. The light intensity was measured by using the photo-diode monitoring circuit at the end of each fiber connected to the veto pulser. The positions of each vertex are the physical locations of each channel on the outside of the pulser box. The red numbers are the labels for the channels and the black are the corresponding fiber #'s and veto panel #'s. The white space is a region where the intensity was not measured.

Part II

Depth and Muon Flux Measurements

Chapter 5

Introduction

We have used part of the CDMS II muon-veto shield to measure the spectrum of muon energy deposition in a scintillator paddle and the rate of muon events. From these measurements, we deduce the depth of the Soudan mine and the muon flux.

The depth in *meters of water equivalent* (m.w.e.) can be estimated if we know the depth in meters and density of the material above the experiment. The unit m.w.e. can be interpreted as either a length-density, or a weight per area (g/cm^2), or the depth under a body of water. This standard has been adopted to allow meaningful comparisons between sites. For CDMS II with an actual depth of $713\,m$, and an average density of $2.80\,g/cm^3$ [10] we find that the depth is $\sim 2000\,m.w.e.$ We will show later that it is possible to make this same measurement without knowing the density of the rock, or the actual depth of the mine.

These measurements were made during a period from June 24th, 2002 through December 2nd, 2002 with a total experimental live time of 2382 hours.

Chapter 6

Experimental Configuration

6.1   Muon telescope

The muon telescope consists of three veto panels of different geometries stacked on top of each other, as shown in Figure 6.1. A larger veto-top panel was on the bottom with an angled side panel sitting across it and a veto-bottom panel on the top. They were stacked this way because we wanted the heaviest panel on the bottom. By using three panels we were able to accomplish two things: 1) remove the γ-ray background by demanding a triple coincidence of an event in each panel, and 2) to test the pulser on the three panel shapes.

6.2   Data Acquisition

The muon-telescope's photo-tubes were held at voltages between 1100-1300V. The anode signals were then buffered through a LeCroy 428f linear fan-in/out NIM module of unity gain. The signals were then sent to a 30 mV discriminator to generate NIM logic pulses. These pulses were digitally ANDed together, with a logic pulse going to the gate of an ADC whenever all three panels fired at the same time. The signal from the bottom panel was split off at the 428f module with one output

Figure 6.1: Digital photo of the muon telescope, also shown is the DAQ electronics with a charge spectrum displayed on the computer.

going to the discriminator, and the other into a channel of the ADC. The ADC was read out using LabView on a MAC which posted the data to the web. The DAQ chain is shown in Figure 6.2. The signal from the bottom panel was delayed before going into the ADC, so that the pulse would arrive during the gate window of 100 ns.
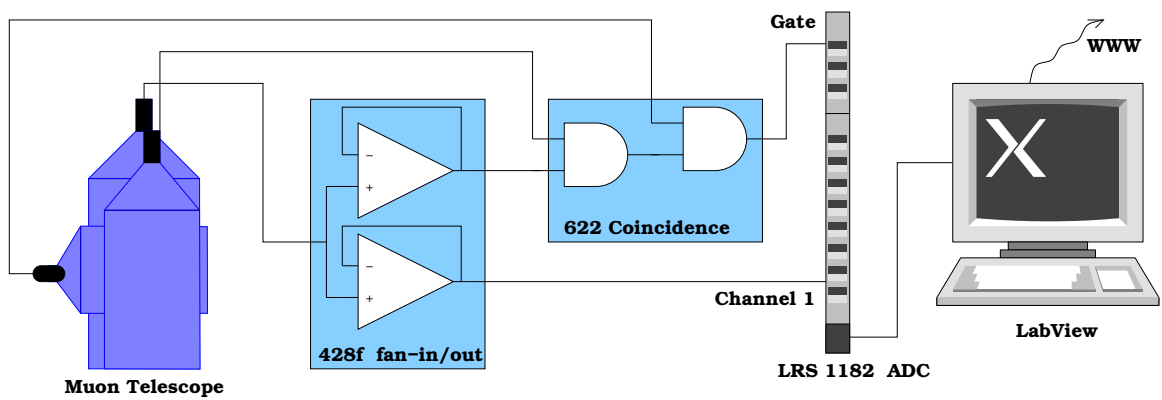
Figure 6.2: The muon telescope data acquisition system. The side and bottom panels run through a unity gain amplifier (*not shown*), and a 30 mV discriminator (*not shown*) before they pass into the coincidence buffer. The top panel is fanned out into two outputs (unity gain), one for the coincidence buffer, the other goes into a channel of the ADC. The output of the coincidence buffer generates the gate for the ADC, which only triggers when all three panels see an event within a 50 ns window.

Chapter 7

Convolution and Landau Theory

7.1 The exponent n

The angular distribution of muons at a given depth, $I(\theta, \phi)$, can be approximated by a power law of the cosine function in θ[11, 12]. Assuming uniformity in ϕ, the azimuthal angle, the flux intensity is then:

$$I(\theta, \phi) = I_v \cdot \cos^n \theta \tag{7.1}$$

where θ is the polar angle measured from vertical, and I_v is the vertical flux intensity at $\cos \theta = 1$. The exponent n depends on the depth and composition of the mine. The origin of this dependence is a so-called 'sec θ' effect: the amount of material in the earth that a muon must successfully penetrate to reach the mine increases as sec θ. As one goes deeper, the fraction of successfully penetrating muons decreases as θ increases. The deeper the mine, the more vertical the muon flux, and the higher n becomes. Empirically Miyake [12] found:

$$n = 1.53 + 8.0 \cdot 10^{-4} \cdot h + \epsilon \tag{7.2}$$

where h is the vertical depth in meters of water equivalent (m.w.e.) and ϵ is a very small correction that arises because of muon decay and ionization losses at very

shallow depths only. Figure 7.1 shows plots of this distribution for different values of n. The important things to notice are that the distribution of muons is proportional to $\cos^n \theta$, and that n increases with depth resulting in a more vertical muon flux.
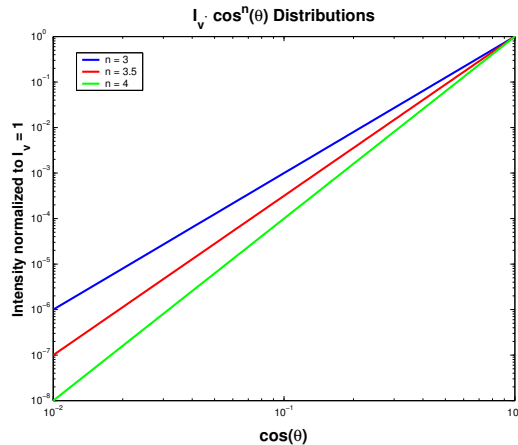
Figure 7.1: These are the expected angular distributions of muons at the depths of 1838 m.w.e. (n = 3), 2463 m.w.e. (n = 3.5), and 3088 m.w.e. (n = 4) with respect to θ, the polar angle. The distribution in ϕ, the azimuthal angle, is assumed to be uniform.

The vertical flux intensity, I_v, was measured with the muon telescope and will be described in more detail in Chapter 9. From the vertical flux intensity the integrated flux can be estimated by integrating $I(\theta, \phi) = I_v \cos^n \theta$ over the upper hemisphere of solid angle; see Appendix B.

7.2   The Landau Distribution

The Landau Distribution represents the distribution of energy loss values for a given charged particle as it passes through a quantity of material. The Landau Distribution is valid for high energy charged particles that pass through a thin material ejecting only a few high energy δ-rays due to ionization losses [13]. It is given

by:

$$\Phi(\lambda) = \frac{\phi(\lambda)}{\xi} \tag{7.3}$$

as shown in figure 7.2, where

$$\phi(\lambda) = \frac{1}{2\pi i} \int_{\sigma-i\infty}^{\sigma+i\infty} \exp\left(s\ln s + \lambda s\right) ds \tag{7.4}$$

where $\sigma > 0$, and $\lambda = \frac{\Delta - \Delta_{mp}}{\xi}$ is the reduced energy variable. Δ is the deposited energy in MeV, ξ is the natural energy loss scale, and Δ_{mp} is the most probable energy and is given by the first term of the Bethe-Bloch formula [14]. The Bethe-Bloch formula describes the average energy loss per path length of a minimum ionizing particle as it passes through a medium.

As a particle passes through thicker material the number of high energy δ-rays starts to increase, eventually causing the distribution to become Gaussian through the central limit theorem. For the muon telescope this will not be the case, as we can show that only a few high energy δ-rays are produced within the scintillator. The natural energy loss scale, ξ, for our muon telescope, is considerably smaller than the maximum deposited energy Δ_{max}, that is, $\frac{\xi}{\Delta_{max}} \ll 0.01$, where $\Delta_{max} = 2m_e c^2 \beta^2 \gamma^2$ from simple relativistic two particle scattering [15]. For the case of a muon with a momentum of $10\,\text{GeV/c}$, for example, $\beta = 0.99994$ and $\Delta_{max} = 9155\,\text{MeV}$. The energy scale is given by $\xi = K(\frac{Z}{A})\frac{\rho}{\beta^2}X$, with $K = 0.154\,\text{MeV/(g-cm}^2)$ for singly charged particles as is the case for muons. $X = l \cdot \sec\theta$ is the path length of scintillator that the particle passed through, where l is the thickness of scintillator. For polyvinyltolulene scintillator ($\langle Z/A \rangle = 0.54155$, $\rho = 1.032\,\text{g/cm}^3$ and $10\,\text{GeV/c}$ muons we find $\xi = 0.4373\,\text{MeV}/\cos\theta$. Then we see that $\frac{\xi}{\Delta_{max}} = 4.77 \cdot 10^{-4}/\cos\theta < 0.01$ for $\cos\theta > 0.005$. The regime where $\cos\theta < 0.005$, only accounts for $100 \cdot (0.005)^{n+1}\%$ of the total probability. These angles can be safely ignored because they are outside of the muon telescope's acceptance. For particles with $\beta \simeq 1$ the most probable energy reduces to $\Delta_{mp} = \xi \ln\left(\frac{1.219 Z^2 X}{a_o}\right)$, where Z is the charge of the incoming particle in electron units, and a_o is the typical Bohr radius. A comprehensive derivation is given by Landau [13].
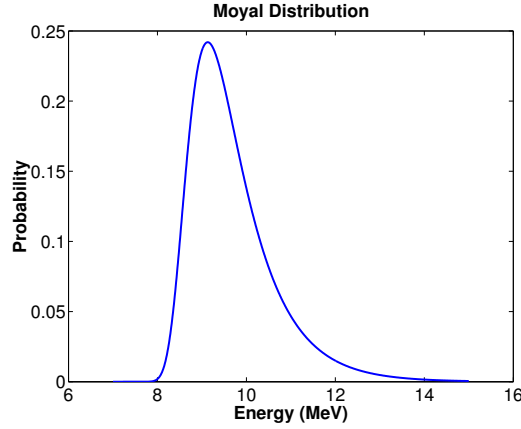
Figure 7.2: The Moyal Distribution that would exist for completely vertical $10\,GeV/c$ minimum ionizing muons passing through $5.08\,cm$ thick scintillator.

There is no known closed form solution to Equation 7.4 though asymptotic solutions can be found for limiting cases (Landau [13]). In 1955 Moyal found a function that closely resembles the Landau Distribution. Working from similar principles, Moyal was able to find a closed form solution for the problem of ionization losses [16]. The normalized Moyal function is given by:

$$f(\lambda) = \frac{1}{\sqrt{2\pi}} e^{\frac{1}{2}(-\lambda + e^{-\lambda})} \tag{7.5}$$

where λ is the reduced energy variable. The benefit of the Moyal function is that it is much easier to work with than the explicit Landau Distribution. Note that $f(\lambda)$ is dependent on the path length through the scintillator. Explicitly in terms of $\cos\theta$, we find:

$$\lambda = \frac{\Delta}{.4373\,MeV} \cos\theta - \ln\left|\frac{1.219 Z^2\,l}{a_o \cos\theta}\right| \tag{7.6}$$

It should also be noted that Moyal's function is *not* a closed form solution to the Landau distribution, but rather an independent solution to the ionization loss problem. Moyal extensively shows where his function and Landau's differ, which is only in a few cases and never by more then a few percent [16]. It is hard to justify the

inclusion of errors that would arise between the two distributions because they are both good solutions to this problem.

7.3 The Principle Variable

The parameters of the Landau and Moyal distributions that we will exploit are the *Full-Width-at-Half-Max* (FWHM) and the peak location. The principle variable S =FWHM/peak, is then dimensionless and independent of linear gain variations. The peak is obviously at Δ_{mp}. Extracting the FWHM from the paramerization is more laborious. First we introduce a Moyal-like function that will be used to fit to the data:

$$f(\alpha, \varphi, \Delta_{mp}, \Delta) = \alpha e^{\frac{1}{2}(-\varphi(\Delta - \Delta_{mp}) + e^{-\varphi(\Delta - \Delta_{mp})})} \tag{7.7}$$

The variables α, φ, and Δ_{mp} are the fitting parameters. The value of the fitting function at the peak is

$$f_{peak} \equiv f(\alpha, \varphi, \Delta_{mp}, \Delta_{mp}) = \alpha e^{-\frac{1}{2}} \tag{7.8}$$

To find the values of Δ when $f(\alpha, \varphi, \Delta_{mp}, \Delta) = \frac{1}{2} f_{peak}$ we take

$$\frac{1}{2}\alpha e^{-\frac{1}{2}} = \alpha e^{\frac{1}{2}(-\varphi(\Delta - \Delta_{mp}) + e^{-\varphi(\Delta - \Delta_{mp})})} \tag{7.9}$$

and then solve for Δ_+ and Δ_- the two solutions to this problem. Unfortunately this has to be solved numerically. Fortunately this is very easy to do even with a pocket calculator. We find that

$$\Delta_+ = \frac{2.285}{\varphi} + \Delta_{mp} \tag{7.10}$$

$$\Delta_- = \frac{-1.306}{\varphi} + \Delta_{mp} \tag{7.11}$$

$$FWHM \equiv \Delta_+ - \Delta_- = \frac{3.59}{\varphi} \tag{7.12}$$

Now we use the expressions for $FWHM$ and Δ_{mp} into S to find

$$S = \frac{FWHM}{\Delta_{mp}} = \frac{3.59}{\varphi \Delta_{mp}} \tag{7.13}$$

This is a nice result because it is completely independent of the normalization parameter, so all that has to be done to a set of data that follows a Landau like distribution is to measure these quantities directly. It is also worthwhile to note that $\varphi = \frac{1}{\xi}$ which is the inverse of the natural energy loss scale defined earlier.

In general, S is relatively independent of all the parameters that are plugged into it. This is due to the logarithmic dependence on the parameters. For a given Landau distribution

$$S = FWHM/\Delta_{mp} = \frac{3.59\xi}{\xi \ln\left(\frac{1.219Z^2X}{a_o}\right)} = \frac{3.59}{\ln\left(\frac{1.219Z^2X}{a_o}\right)} \tag{7.14}$$

which for 5.08 cm thick scintillator and $Z = 1$ yields $S = 17.2\%$. Even by varying the parameters quite a bit, S never changes by more than a few percent.

7.3.1   Statistical Uncertainties

The statistical uncertainty for the measurement S we will define as dS. The uncertainty, dS, is going to be a function of the fitting parameters φ, and Δ_{mp}, and their uncertainties; α and its uncertainty do not effect S in any meaningful way. Error propagation gives:

$$\delta S = \left(\frac{\partial S}{\partial \varphi}\right)\delta\varphi + \left(\frac{\partial S}{\partial \Delta_{mp}}\right)\delta\Delta_{mp} \tag{7.15}$$

Since $\langle\delta\varphi\rangle = 0 = \langle\delta\Delta_{mp}\rangle$, or that random fluctuations integrated over an ensemble of events tend to die out, we will need to use the squares of these fluctuations to find the error. Squaring Equation 7.15 and taking the expectation value we find:

$$\langle\delta S^2\rangle = \left(\frac{\partial S}{\partial \varphi}\right)^2\langle\delta\varphi^2\rangle + \left(\frac{\partial S}{\partial \Delta_{mp}}\right)^2\langle\delta\Delta_{mp}^2\rangle + 2\left(\frac{\partial S}{\partial \varphi}\right)\left(\frac{\partial S}{\partial \Delta_{mp}}\right)\langle\delta\varphi\,\delta\Delta_{mp}\rangle \tag{7.16}$$

After taking a few partial derivatives it is straight forward to show that the statistical error of S is

$$dS \equiv \sqrt{\langle \delta S^2 \rangle} = \frac{3.59}{\varphi \Delta_{mp}} \left(\frac{\langle \delta \varphi^2 \rangle}{\varphi^2} + \frac{\langle \delta \Delta_{mp}^2 \rangle}{\Delta_{mp}^2} + 2 \frac{\langle \delta \varphi \, \delta \Delta_{mp} \rangle}{\varphi \Delta_{mp}} \right)^{\frac{1}{2}} \quad (7.17)$$

To find the squared fluctuations associated with the fit, we need to find the covariance matrix, C, associated with the fitting parameters.

$$C \quad = \quad \begin{pmatrix} \langle \delta \alpha^2 \rangle & \langle \delta \varphi \, \delta \alpha \rangle & \langle \delta \Delta_{mp} \, \delta \alpha \rangle \\ \langle \delta \alpha \, \delta \varphi \rangle & \langle \delta \varphi^2 \rangle & \langle \delta \Delta_{mp} \, \delta \varphi \rangle \\ \langle \delta \alpha \, \delta \Delta_{mp} \rangle & \langle \delta \varphi \, \delta \Delta_{mp} \rangle & \langle \delta \Delta_{mp}^2 \rangle \end{pmatrix}$$

From this we can then plug these parameters into Equation 7.17 to get the statistical error. Note that $\langle \delta \varphi \, \delta \Delta_{mp} \rangle = \langle \delta \Delta_{mp} \, \delta \varphi \rangle$ since these quantities *must* be real.

7.4 Convolution

The obvious way to measure depth by using the muon flux is to simply compare the measured rate to what other experiments have measured and extrapolate a depth. Another possibility is to measure the surface and underground rates and then infer the amount of material between the two detectors from the difference in rates. We will justify the use of a new method that involves measuring the shape of the energy deposition spectrum of the muon flux.

The basic idea is that the width of the pulse charge spectrum from the scintillator is sensitive to the exponent, n, in the power law spectrum of the muon flux intensity, Equation 7.1. The shape of the pulse charge spectrum will be determined by a convolution of a Moyal function, Equation 7.5, with this angular distribution [17]. Because the Moyal function is dependent on $\cos \theta$.

This convolution, $C(\Delta, n)$, is the integral of the Moyal function, weighted with a normalized cosine power function $(n + 1) \cos^n \theta$:

$$C(\Delta, n) = \int_0^1 \frac{(n+1)}{\sqrt{2\pi}} \cos^n \theta e^{\left(-\frac{1}{2}\lambda + e^{-\lambda}\right)} d(\cos \theta) \quad (7.18)$$
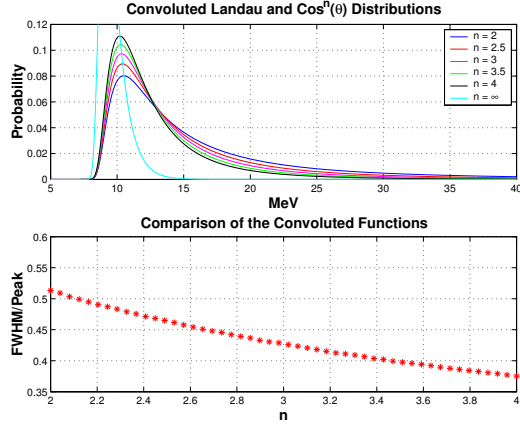
Figure 7.3: The convolution of a Landau distribution with a cosine power function for various values of n (upper panel), and $S = FWHM/\Delta_{mp}$ as a function of n (lower panel).

Where λ, defined by Equation 7.6, is a function of Δ and $\cos\theta$. This integral has to be solved numerically and is shown in Figure 7.3 for various values of n. The effect of the convolution leads to a broadening of the Moyal distribution, and a larger Δ_{mp}. However, as n increases (one goes deeper), the energy deposition spectrum gets narrower. This demonstrates that it is possible to measure S from a distribution and then consequently measure n and the depth in m.w.e. For the $S(n)$ relation shown in figure 7.3, we find:

$$n = 54.4\,S^2 - 62.5\,S + 19.8 \tag{7.19}$$

which leads to

$$h = \frac{54.4\,S^2 - 62.5\,S + 18.3 - \epsilon}{8} \cdot 10^4 \tag{7.20}$$

the depth in m.w.e.. This fit is quite good, so it is justifiable to ignore the errors associated with this relation because the errors in the fit associated with the data set are going to be much larger than this error. Therefore, by measuring S we can immediately get both n and the depth.

Chapter 8

Raw Data

The muon telescope, described in Section 6.1, was set up in the Soudan Iron Mine at the 27$^{\text{th}}$ level ($\sim 713\ m$ below the surface). Data were taken over a six month period, from June 24$^{\text{th}}$ 2002 through December 2nd 2002, in order to observe enough events to make a statistically significant measurement. Muon events were characterized by demanding a triple coincidence between the three scintillator panels of the telescope. The hope was that any other sources of events, electrons from Compton scattering of γ-rays for example, would not be energetic enough to penetrate through three 2" thick panels. The only worry from the γ-rays is the rare occurrence of an accidental coincidence; this is more thoroughly described in Section 9.3, and turns out to be a very small number of events.

The data read out were the total charge of the photo-tube pulse for each event, and the time it took to record every 16 events. This produced a charge spectrum of events with a corresponding total live time. The entire readout Data Acquisition chain is described in Section 6.2.

Due to a computer crash the data were taken in two runs. During the second run it became obvious that the data had shifted from its original position. We attribute this to a shift in the pedestal of our LeCroy 428f NIM module. To correct for this change in pedestal, we measured the pedestal of the second data

set and adjusted the position on the first data set with the method described in Section 8.1. This enabled us to combine both data sets together when for the depth measurement.
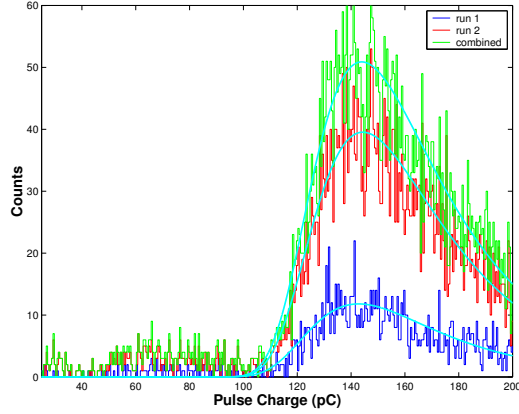
Figure 8.1: Here are the two sets of raw data, after the first set has been shifted by changing the pedestal in order to minimize the χ^2 between the two sets.

8.1   Combining Data sets

In order to find the pedestal of the first data set, we need to align the two data sets. We chose to use a χ^2 minimization technique to align the muon peaks of the two distributions. This method is better than simply aligning the peaks of the distributions because it uses more than just one point of data to find the pedestal. By varying the pedestal of the first data set and then calculating χ^2, Equation 8.1, we found a minimum which corresponds to the best alignment of the two data sets, see Figure 8.2.

$$\chi^2 = \sum_i^{bins} \frac{(X_2(i) - X_1(i))^2}{\sigma_i^2} \tag{8.1}$$

where $X_j(i)$ are the values of data set j, at bin i, and σ_i^2 is the error between each of the two sets at bin i. We believe the gain was stable during the measurements, and need not be corrected for.

After finding the change in the pedestal that corresponds to the minimum of the curve in Figure 8.2, we simply shift each bin of the first data set in order to align with the second data set. The combined data sets are shown in figures 8.1 and 8.3.
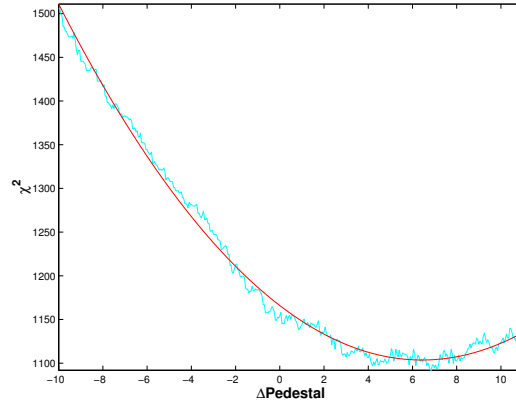
Figure 8.2: By varying the pedestal of the fit data set across the range shown, taking the χ^2 difference between the distributions, and fitting a parabola to the distribution, it was possible to find the minimum value of χ^2 which corresponds to the true shift of the pedestal.

8.2   Fits

For the charge distributions shown in Figure 8.1 the fits were done with the function Equation 7.7. Only data with pulse charge greater than $100\,\mathrm{pC}$ were fit, so that the low charge events would not interfere with the fit. Consequently, it is also valuable to try to understand what these low charge events actually are. The few 10's of events below $40\,\mathrm{pC}$ have an energy consistent with the γ-ray background. These events may be accidental coincidences. In Section 9.3 I will discuss how to estimate the number of these events and how they affect the flux measurement and the error.

The events between $40-100\,\mathrm{pC}$ are most likely events that pass through the

edge of the scintillator which causes the amount of charge recorded to be significantly reduced.

8.3 Depth Analysis

As was described in Section 7.3, it is fairly easy to get the principle variable, $S = \text{FWHM}/\Delta_{mp}$, out of the fit. The Moyal fit was done using a *non-linear-least-squares* fitting routine similar to the method used to combine the two data sets (a χ^2 minimization technique). The fitting routine outputted the central values α, φ, and Δ_{mp} along with the covariance matrix associated with these parameters. The dominant error in S comes from the uncertainty of Δ_{mp}, the peak location, which dominates by a factor of about 2800 over that of φ, the inverted natural energy loss scale. The derived exponent, n, and the derived depth, h, are then extracted simply from S as was described in Section 7.4. The error propagation from S is described in the next section. The combined data sets and the statistics are shown in Figure 8.3. The results are summarized in Table 8.1.
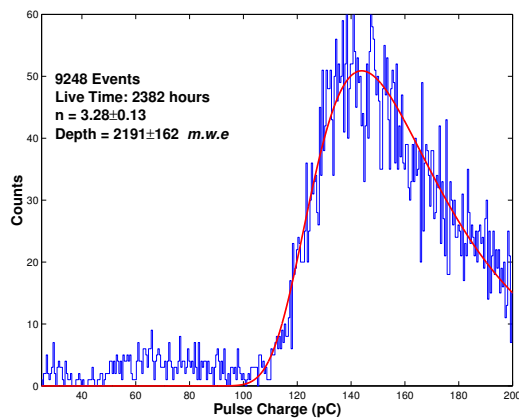
Figure 8.3: The Muon Energy Deposition Spectrum after the combination of the two data sets.

8.4   Depth Errors

We use Equation 7.17 to evaluate the statistical error in our measurement. Then using Equations 7.19 and 7.20 to find the exponent and the depth we can find the error on n and on the depth. Starting with Equation 7.19 or

$$n = 54.4\, S^2 - 62.5\, S + 19.8 \tag{8.2}$$

since $n(S)$ is a function of one variable, the error propagation is simply

$$dn \equiv \sqrt{\delta n^2} = \left| \frac{\partial n}{\partial S} \right| dS \tag{8.3}$$

By inserting dS from Equation 7.17 we find

$$
\begin{aligned}
dn &= \left| 108.8\, S - 62.5 \right| dS \\
&= \left| \frac{390.6}{\varphi \Delta_{mp}} - 62.5 \right| \frac{3.59}{\varphi \Delta_{mp}} \left(\frac{\langle \delta \varphi^2 \rangle}{\varphi^2} + \frac{\langle \delta \Delta_{mp}^2 \rangle}{\Delta_{mp}^2} + 2 \frac{\langle \delta \varphi\, \delta \Delta_{mp} \rangle}{\varphi \Delta_{mp}} \right)^{\frac{1}{2}}
\end{aligned}
\tag{8.4}
$$

Since the depth, h, is proportional to n. The error on h is just $dh = 1.25 \cdot 10^3\, dn$. The results are summarized in Table 8.1.

Table 8.1: Summary of the statistics extracted from the data in Figure 8.3. Included are the fit parameters used in Equation 7.7, the covariance matrix described in Section 7.3.1 , and our final results for the depth.

Parameter	Value	Units
Events	9248	—
Duration	2382	hours
α	83.9091	—
φ	0.060754	pC^{-1}
Δ_{mp}	143.9629	pC
C	$\begin{pmatrix} 2.19 & 0.00116 & -0.222 \\ 0.00116 & 1.37 \cdot 10^{-6} & -0.0003 \\ -0.222 & -0.0003 & 0.1735 \end{pmatrix}$	
FWHM	59.09	pC
S	0.411 ± 0.007	—
n	3.28 ± 0.13	—
Depth	2191 ± 162	m.w.e.

Chapter 9

Muon Flux Measurement

9.1 Monte Carlo

Since the muon telescope is not a simple horizontal sheet we perform Monte Carlo simulation of muon tracks through it to determine the acceptance so that we may extract the flux. To do so we start with N muons distributed randomly across an area A_g that is the overlap of the panels. We will use the bottom surface of the top panel ensuring that any muon that passes through all three panels has to pass through this area. The muons are then generated from a $\cos^{4.28}\theta$ distribution in the polar angle, which is the result of $\cos^n \theta$ from the flux intensity with $n = 3.28 \pm 0.13$ as shown in Table 8.1, and an additional factor of $\cos\theta$ to arrive at a *horizontal* flux, as described in Appendix B. The generated distribution is shown in Figure 9.1.

We retain all muon tracks that successfully pass through all three panels. This gives us a number, n, of muon tracks that are accepted. The expected rate through the area A_g is $R_{A_g} = \Phi_\mu \cdot A_g$, where Φ_μ is the downward flux integrated over the 2π steradians above the area. Not every muon incident upon the A_g successfully penetrates all three muon detectors in the telescope. The rate through all three paddles, R_3, is

$$R_3 = \Phi_\mu \cdot A_g \, \frac{n}{N} \tag{9.1}$$
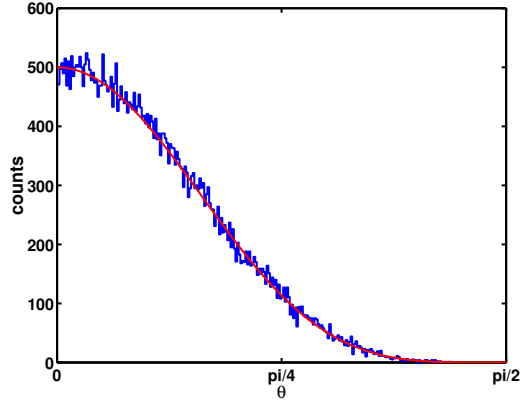
Figure 9.1: The blue histogram is the Monte Carlo of 50000 events from a $\cos^{4.28}\theta$ distribution. Overlaid in red is the $\cos^{4.28}\theta$ function itself, for comparison.

where $\left(\frac{n}{N}\right)$ can be thought of as the success fraction, or as an acceptance.[18] If we set Equation 9.1 equal to the measured rate through the three panels then we can estimate Φ_μ by

$$\Phi_\mu = R_3 \left(\frac{N}{n}\right) \frac{1}{A_g} \tag{9.2}$$

The results of the Monte Carlo for the factor $\left(\frac{n}{N}\right)$ are listed in Table 9.1.

9.2 Φ_μ

Taking Equation 9.2 as the integrated flux we can solve for the vertical flux intensity, I_v. Following Appendix B, we see that

$$I_v(\theta, \phi) = I_v \cos^n \theta \tag{9.3}$$

By inserting this into Equation B.4 we find how to convert between the Intensity and the flux to get

$$\Phi_\mu = \int_{2\pi} I_v \cos^{n+1} \theta d\Omega = I_v \frac{2\pi}{n+2} \ sr^{-1} \tag{9.4}$$

which yields the result of $\Phi_\mu = 1.19\, I_v \ sr^{-1}$ for our case of $n = 3.28$. See Table 9.2 for the summary of the results.
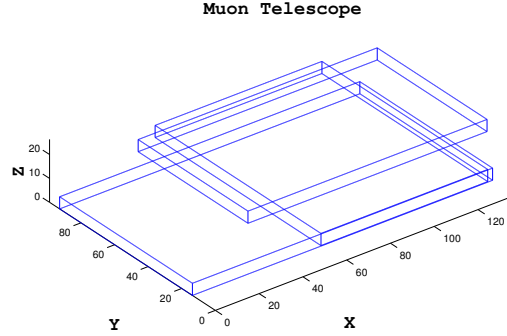
Figure 9.2: The physical shape of the muon telescope shown in Figure 6.1 used for the Monte Carlo, only the scintillator is shown. The triangular light guides and PMT's are omitted in this drawing

9.3 Flux Errors

To find the errors on the integrated flux, Equation 9.2, we need to understand the errors on the individual independent variables; the rate $R_3 = c/t$, the generation area A_g, and the Monte Carlo N/n. Following the procedure outlined in Section 7.3.1 the error on Φ_μ is:

$$d\Phi_\mu \equiv \sqrt{\langle \delta\Phi_\mu^2 \rangle} = \tag{9.5}$$

$$\left(\left(\frac{\partial\Phi_\mu}{\partial c}\right)^2 \langle \delta c^2 \rangle + \left(\frac{\partial\Phi_\mu}{\partial t}\right)^2 \langle \delta t^2 \rangle + \left(\frac{\partial\Phi_\mu}{\partial A_g}\right)^2 \langle \delta A_g^2 \rangle + \left(\frac{\partial\Phi_\mu}{\partial\left(\frac{N}{n}\right)}\right)^2 \underbrace{\langle \delta\left(\frac{N}{n}\right)^2 \rangle}_{\to 0 \text{ as } N\to\infty} \right)^{\frac{1}{2}}$$

where c is the number of counts, t is the live time of the experiment, A_g is the generation area of the Monte Carlo, and $\left(\frac{N}{n}\right)$ is the ratio of generated to kept events from the Monte Carlo. The cross terms that should be in Equation 9.5 are assumed to be zero because the variables are completely uncorrelated. After taking all the necessary partial derivatives, Equation 9.5 becomes:

$$d\Phi_\mu \equiv \sqrt{\langle \delta\Phi_\mu^2 \rangle} = \tag{9.6}$$

$$\left(\left(\frac{1}{t}\left(\frac{N}{n}\right)\frac{1}{A_g}\right)^2 \langle \delta c^2 \rangle + \left(\frac{c}{t^2}\left(\frac{N}{n}\right)\frac{1}{A_g}\right)^2 \langle \delta t^2 \rangle + \left(\frac{c}{t}\left(\frac{N}{n}\right)\frac{1}{A_g^2}\right)^2 \langle \delta A_g^2 \rangle \right)^{\frac{1}{2}}$$

The $\langle \delta \left(\frac{N}{n} \right)^2 \rangle$ term in Equation 9.5 is negligible because for the Monte Carlo (MC) simulation of $1.5\,M$ events the statistical error of the number n is much less then the statistical error in measuring only 9248 events. As can be seen in Table 9.1, the percent fluctuation in the 30 MC runs is roughly 0.3% for 50000 events. Since we are combining *all* the sets the error reduces even more, and it can therefore be justifiably ignored. By varying the exponent in the MC by 1σ, $\left(\frac{N}{n} \right)$ changes by only 0.12%, which further justifies ignoring the $\langle \delta \left(\frac{N}{n} \right)^2 \rangle$ term.

The error, $\langle \delta c^2 \rangle$, is from two sources. The first is Poisson; $\sigma_{Poisson} = \sqrt{c}$. The second is due to accidental γ-ray coincidence in the telescope. This can be estimated by finding the probability of a triple coincidence within the $50\,ns$ coincidence buffer time window. We can find this error by finding the probability of no coincidence from the Poisson distribution:

$$P = \sum_{n=0}^{\infty} \frac{\lambda^n e^{-\lambda}}{n!} \tag{9.7}$$

where $\lambda = rate \cdot (time\ interval)$ is the mean of the Poisson distribution. The first term of this sum is the probability of having zero events, or $P(0) = e^{-\lambda}$. Now if we want to know the probability of an event in two panels, we take $P(n \geq 1) = 1 - e^{-\lambda}$. For three panels, we simply square this number to find $P_{\text{accidental}} = (1 - e^{-\lambda})^2$. For a γ-ray singles rate of $200\,\text{Hz}$, and a window of $50\,\text{ns}$, we find $P_{accidental} \approx 10^{-10}$. To find the total number of expected accidental coincidences we take $N_{\text{accidental}} = rate \cdot t \cdot P_{\text{accidental}}$, where t is the total live time, and we find $N_{\text{accidental}} = 0.17$ events. This small number of events is inconsequential and can be safely ignored. In Section 8.2 I claimed that the events below $10\,\text{pC}$ in Figure 8.1 were likely to be accidental coincidences. As we can see this is not actually the case. These events may be caused other physics processes, such as double Compton scatters from the γ-ray background. They may even be more of these edge events. Either way, they are not significant and hardly affect the results.

The data is readout in groups of 16 events. The time is measured by how long it takes to fill the buffer of the ADC. Therefore the number of times

that the time is recorded is $c/16$. There is an uncertainty associated with the time measurement because we don't trust the clock on the computer, that we will assign to be $\approx 1s$. Since we do not know how this uncertainty takes place, whether it randomly fluctuates about a mean or whether it adds in the same direction every time, we will conservatively assign a large error. If the clock added a second every measurement, then the most we would be off is by $(c/16)1\,s$. Therefore, we will call the error of the time measurement $\langle \delta t^2 \rangle = (c/16)^2\,\mathrm{s}^2$.

The area of generation, A_g, can be found by measuring the bottom of the top most panel in Figure 9.2. For this we assigned a 1/4" error to the measurement of each side, corresponding to an error in A_g of $dA_g = 0.008\,\mathrm{m}^2$.

For I_v we can invert Equation 9.4 and take some partial derivatives to find

$$
\begin{aligned}
dI_v &= \left(\left(\frac{\partial I_v}{\partial \Phi_\mu} \right)^2 \langle \delta \Phi_\mu^2 \rangle + \left(\frac{\partial I_v}{\partial n} \right)^2 \langle \delta n^2 \rangle \right)^{\frac{1}{2}} sr \\
&= \left(\left(\frac{n+2}{2\pi} \right)^2 \langle \delta \Phi_\mu^2 \rangle + \left(\frac{\Phi_\mu}{2\pi} \right)^2 \langle \delta n^2 \rangle \right)^{\frac{1}{2}} sr
\end{aligned}
\tag{9.8}
$$

All the flux results summarized in Table 9.2.

9.3.1   Systematic Errors

We have presented a new method to measure depth by measuring the shape of the deposited energy spectrum into a piece of scintillator. Our result of $2192 \pm 162\,\mathrm{m.w.e.}$ is consistent with the naive expectation of $2000\,\mathrm{m.w.e.}$ Through a measurement of the rate of muon events and a simple acceptance Monte Carlo simulation we were able to extract the flux. The rate in our detector is *not* very sensitive to the angular distribution as long as the rate is mostly vertical.

The Soudan II experiment which shares our mine has also measured the muon flux there. They quote $\Phi_\mu = 1.80 \times 10^{-3} \mathrm{m}^{-2} \mathrm{s}^{-1}$ and $I_v = 1.03 \times 10^{-3} \mathrm{m}^{-2} \mathrm{s}^{-1} \mathrm{sr}^{-1}$ with errors of 5% [19]. Our results for Φ_μ are lower than those of Soudan II by about

20%, or about 4 statistical standard deviations (σs). Our results for I_v are lower than those of Soudan II by 80%, or about 11 statistical standard deviations.

There exist several plausible explanations for this discrepancy. Perhaps either the Soudan II measurement has much larger systematics then they quote, or our measurement does. For the Soudan II measurement we could not find any details as to how this measurement was made.

One curious aspect of the Soudan II measurement is is the ratio of the flux to vertical flux intensity. Equation 9.4 shows the ratio of Φ_μ to I_v should be:

$$\frac{\Phi_\mu}{I_v} = \frac{2\pi}{n+2} \, \text{sr}^{-1}. \tag{9.9}$$

This ratio is $\Phi_\mu/I_v = 1.75 \, \text{sr}^{-1}$ indicates an n of about 2.6, or a depth of about 1330 m.w.e., which is substantially different than our result for the mine depth or the simple estimate for mine depth. The Soudan II muon flux is not as vertical as expected for this depth, which explains why the discrepancy between our I_v measurement and Soudan II's is greater than the discrepancy between the Φ_μ values.

If we look back on Figure 8.3, we see that there are a number of events below 100 pC that are unexplained. As we have shown they are not consistent with accidental coincidences due to γ-rays. Our assumption that they are muons that somehow graze the edge of our scintillator may be wrong, however. These events might be a rare background of high energy γ's, or electrons. They may not be muons and in that case should not be included in the muon flux measurement. If we just subtract off these 425 events our flux reduces to $\Phi_\mu = 2.1 \times 10^{-3} \text{m}^{-2}\text{s}^{-1}$, with $I_v = 1.77 \times 10^{-3} \text{m}^{-2}\text{s}^{-1}\text{sr}^{-1}$, which is still inconsistent with Soudan, although Φ_μ is within 3σ. We believe that the events are muons but we will assign a systematic error that covers the possibility that they are not, and we include that as the second error in our final result in Table 9.3.

Our measurements will be repeated with the entire CDMS II veto system in the near future, which should resolve the discrepancies we note here.

Table 9.1: The Monte Carlo results for the geometric flux through the muon telescope in Figure 9.2. The tracks were selected randomly from a $\cos^{4.28}\theta$ distribution, where θ is the elevation angle, and uniformly in azimuth from a random point on the generation area which was chosen to be the bottom surface of the top panel of the telescope.

	N	n
	50000	34110
	50000	34108
	50000	34039
	50000	34145
	50000	33976
	50000	34171
	50000	34252
	50000	34195
	50000	34127
	50000	34182
	50000	34166
	50000	34126
	50000	34326
	50000	34016
	50000	34112
	50000	34390
	50000	34037
	50000	34288
	50000	34239
	50000	34200
	50000	34278
	50000	34171
	50000	34209
	50000	34073
	50000	34236
	50000	34184
	50000	34272
	50000	34009
	50000	34381
	50000	34100
totals	1500000	1025118

Table 9.2: The results for Φ_μ and I_v, not including systematics.

Variable	Value	Uncertainty	Units
R_3	1.078	± 0.011	10^{-3} s^{-1}
$\left(\frac{N}{n}\right)$	1.464	—	—
A_g	0.714	± 0.008	m^2
Φ_μ	2.209	± 0.034	10^{-3} m^{-2} s^{-1}
I_v	1.857	± 0.054	10^{-3} m^{-2} s^{-1} sr^{-1}

Table 9.3: The results for Φ_μ and I_v including systematic errors associated with a possibly unknown source of events in Figure 8.3.

Variable	Value	Uncertainty	Units
Φ_μ	2.21	$\pm 0.03^{+0.00}_{-0.10}$	10^{-3} m^{-2} s^{-1}
I_v	1.86	$\pm 0.05^{+0.00}_{-0.08}$	10^{-3} m^{-2} s^{-1} sr^{-1}

Chapter 10

Conclusions

We have successfully completed all of the criteria that were set for the veto pulser, and have created a device that can remotely calibrate the veto shield. We have shown this device to be stable to $\sim 3\%$. We now leave this device in the highly capable hands of the CDMS collaboration to use during their searches for dark matter.

By introducing a new technique to measure depth, we have measured both the depth of the Soudan mine in m.w.e. and the exponent of the angular distribution of muons. We found our result of 2191 ± 162 m.w.e. to be 1σ away from the naive expectation of 2000 m.w.e.. We also have measured the muon flux in the Soudan Mine, with results summarized in Table 9.3.

These results will allow constraint of the rate of backgrounds due to neutrons created by muon interactions in the materials surrounding the CDMS II experiment. These neutrons, in turn, are one of the most likely backgrounds in the search for WIMP dark matter with CDMS II.

54

Appendix A

Blue Light Pulser Schematics

Here are most of the relevant drawings associated with the CDMS II Veto Pulser.
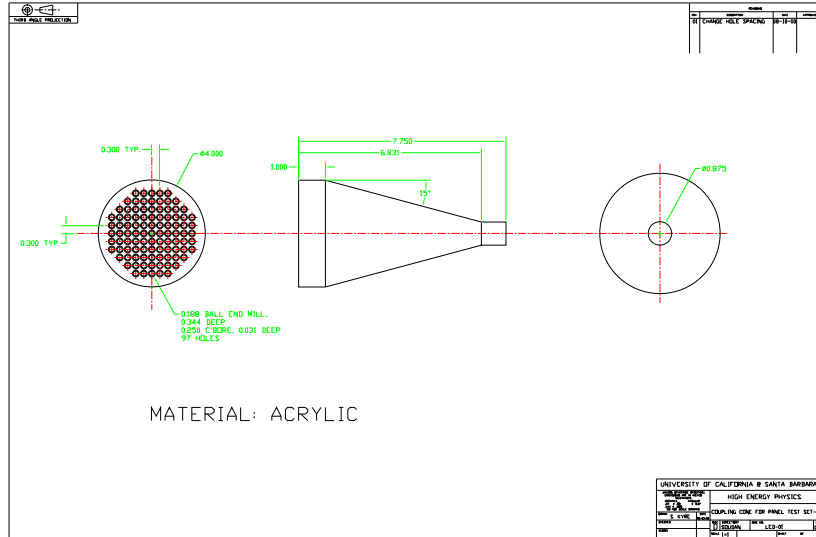
Figure A.1: Detailed drawing of the acrylic cone used to mix the light from 97 blue LEDs.
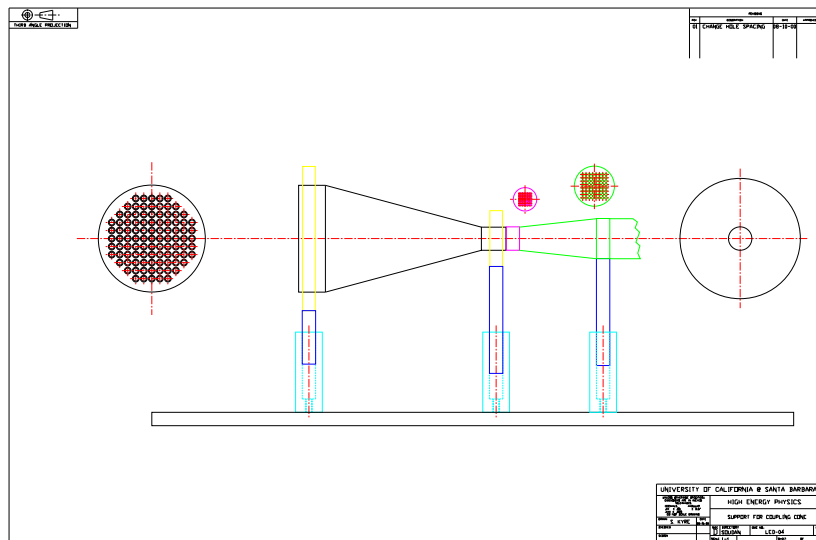
Figure A.2: Drawing of the acrylic cone sitting in its mounts coupled to the 56 fibers. The smaller acrylic collar which couples to the acrylic cone has been exchanged with an aluminum one with a different hole spacing, as shown in Figure A.3.

Ø0.875
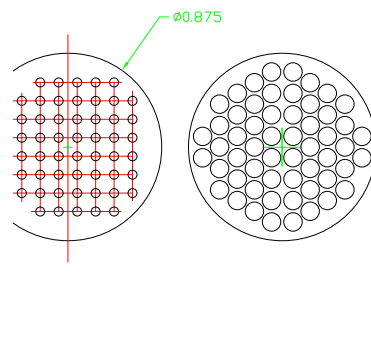
Figure A.3: The aluminum collar that couples the 56 fibers to the acrylic cone, the holes are tapered so that the fiber cladding could securely epoxy to the collar. Also shown is the original acrylic collar spacing for comparison.

58

Figure A.4: This circuit is designed to drive ≈ 6 amps of current to the 97 blue LEDs. The circuit is controlled via a digital 0-5V line that triggers the one-shot to generate 100 ns pulses through an op-amp to dump current through a MOSFET to the LEDs.
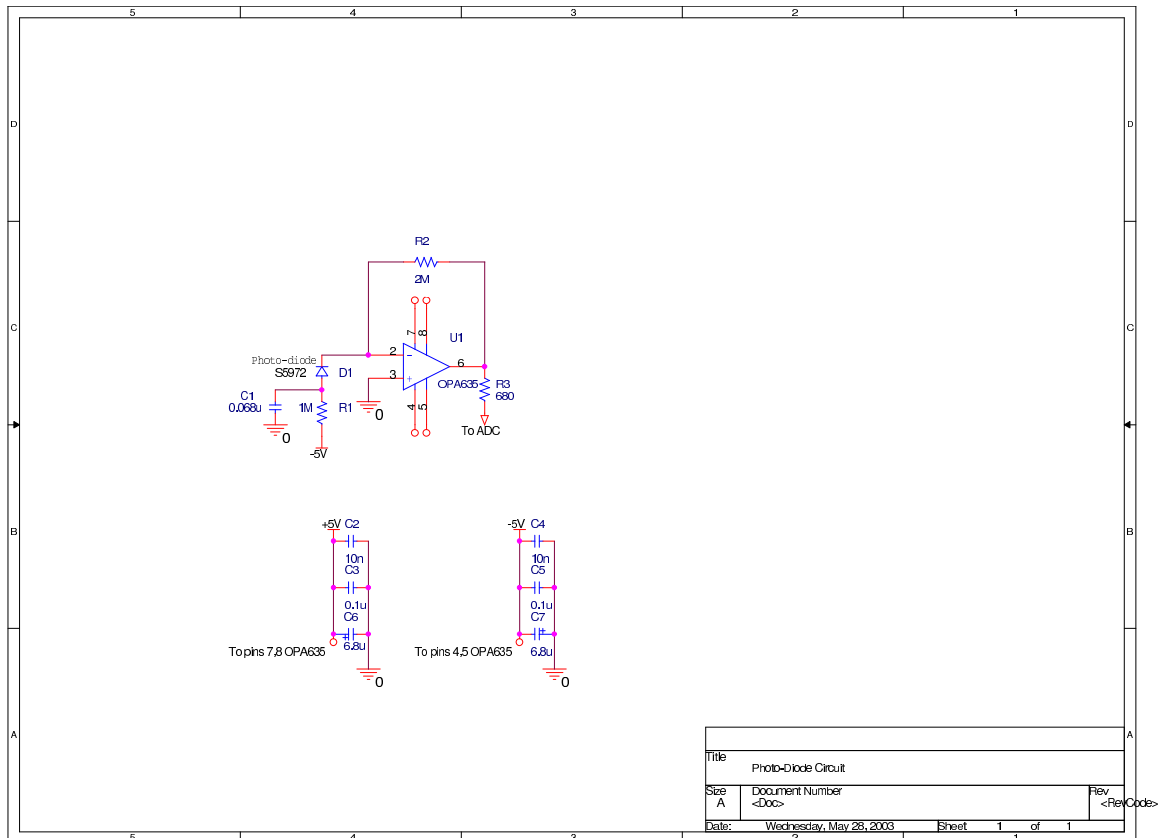
Figure A.5: This circuit is designed to monitor the light output of the pulser. It uses Hamamatsu S5972 photo-diodes [7] that have been mounted inside of the fiber connector. It has been designed so that the pulses can be digitized after very little processing.

Appendix B

Differential Flux

The intensity [11], I, of muons through a differential area, dA, and through a differential solid-angle, $d\Omega$, is given by

$$I \equiv \frac{dN}{dt\,dA\,d\Omega} \tag{B.1}$$

Where dN/dt is the rate measured. This area is perpendicular to the direction of a given incident muon, so then the intensity through a horizontal surface is then given by

$$I = \frac{dN}{dt\,dA'\,d\Omega}\cos\theta \tag{B.2}$$

Where dA' is the horizontal area, and θ is the angle measured from vertical. The *Vertical Flux Intensity*, I_v, is evaluated at $\cos\theta = 1$ so that:

$$I_v \equiv \frac{dN}{dt\,dA'\,d\Omega}(\cos\theta = 1) \tag{B.3}$$

The total integrated flux over the 2π steradian above a horizontal surface is just the integral of the intensity

$$\Phi = \int_{2\pi} I(\theta,\phi)\,d\Omega = \int_{2\pi} I_v(\theta,\phi)\cos\theta\,d\Omega \tag{B.4}$$

Bibliography

[1] D.N. Spergel *et al.*, "First Year Wilkinson Microwave Anisotropy Probe (WMAP) Observations: Determination of Cosmological Parameters," submitted to *Ap. Jour.* (astro-ph/0302209) 2003.

[2] T. Saab, "Search for Weakly Interacting Massive Particles with the Cryogenic Dark Matter Search Experiment," Ph. D. Thesis Stanford University, 2002, (unpublished).

[3] D.S. Akerib *et al.*, "New Results from the Cryogenic Dark Matter Search Experiment," submitted to *Phys. Rev. Lett.* (hep-ex/0306001) June, 2003. Preprint.

[4] R. Bernabei *et al.*, "Search for WIMP Annual Modulation Signature: Results from DAMA/NaI-3 and DAMA/NaI-4 and the Global Combined Analysis," *Phys. Lett.* **B480**, 23 (2000).

[5] A. Benoit *et al.*, "Improved Exclusion Limits from the EDELWEISS WIMP Search," *Phys. Lett.* **B545**, 43 (2002).

[6] Saint-Gobain Crystals and Detectors, at URL `http://www.bicron.com`.

[7] Hamamatsu Corporation, at URL `http://www.hamamatsu.com`.

[8] Nichia America Corporation, at URL `http://www.nichia.com`.

[9] Tyco Electronics Ltd., at URL `http://www.tycoelectronics.com`.

[10] S. Eichblatt, Estimating the Neutron Background from Natural Radioactivity in the Soudan Mine, CDMS Internal Note 97-01-25 (unpublished).

[11] O.C. Allkofer and P.K.F. Grieder, *Cosmic Rays on Earth*, Volume 25-1, Fach-informationszentrum, Germany, 1984.

[12] S. Miyake, "Rapporteur Paper on Muons and Neutrons," *PICRC*, **5**, 1973.

[13] L. Landau, "On the Energy Loss of Fast Particles by Ionization," *J. Phys. USSR*, 8, 1944.

[14] Particle Data Group, "Passage of Particles Through Matter," *Phys. Rev.* **D 66** 2002.

[15] F. Sauli, "Principles of Operation of Multiwire Proportional and Drift Chambers," *Academic Training Program of CERN*, 1977.

[16] J.E. Moyal, "Theory of ionization fluctuations," *Phil. Mag.*, **46** 263 (1955).

[17] H.N. Nelson, Private Communication.

[18] S.J. Yellin, Private Communication.

[19] K. Ruddick, "Underground Particle Fluxes in the Soudan Mine, *NuMi-L-210*, September 1996 (unpublished).